LASER & PHOTONICS REVIEWS
www.lpr-journal.org

Tip-Enhanced Imaging and Control of Infrared Strong Light-Matter Interaction

Yueying Wang, Samuel C. Johnson, Nishant Nookala, John F. Klem, Samuel R. Turner, Richard L. Puro, Min Hu, Igal Brener, Eric A. Muller, Alexey Belyanin,* Mikhail A. Belkin,* and Markus B. Raschke**

Optical antenna resonators enable control of light-matter interactions on the nano-scale via electron–photon hybrid states in strong coupling. Specifically, mid-infrared (MIR) nano-antennas coupled to saturable intersubband transitions in multi-quantum-well (MQW) semiconductor heterostructures allow for the coupling strength to be tuned through antenna resonance and field intensity. Here, tip-enhanced nano-scale variation of antenna-MQW coupling across the antenna is demonstrated, with a spatially-dependent coupling strength g_{aq} varying from 73 (strong coupling) to 24 cm^{-1} (weak coupling). This behavior is modeled based on the spatially dependent local constructive and destructive interference between tip and antenna fields. Using a quantum-mechanical density-matrix model of the MQW system with its designed values of transition dipole moment, doping density, and population decay time, the picosecond IR pulse coupling to intersubband transitions and the associated tip induced strong-field saturation effects are described. These results present a new regime of nonlinear IR light-matter control based on the dynamic manipulation of quantum hybrid states on the nanoscale and in the infrared, with a perspective regarding extension to molecular vibrations.

1. Introduction

Resonant interaction between a quantum system and an optical cavity mode can lead to hybrid light-matter states. When the energy exchange rate exceeds the total dissipation rate, strong coupling gives rise to the formation of two energy eigenstates, separated by the Rabi splitting.[1–4] These hybrid states present new possibilities for applications such as single-molecule observability,[5–8] single photon emitters,[9] and low-threshold solid-state lasers.[10] Strong coupling depends on the transition dipole strength of the quantum system, total loss rate, and the mode volume of the optical cavity. With diffraction-limited mode volumes, even for high Q-factor resonators, the strong coupling of a single quantum emitter has historically necessitated operation at cryogenic temperatures[11,12] to counteract dissipation.[13–16]

Plasmonic nano-resonators with deep sub-diffraction limited mode volumes as

Y. Wang, S. C. Johnson, S. R. Turner, R. L. Puro, M. B. Raschke
Department of Physics and JILA
University of Colorado
Boulder, CO 80309, USA
E-mail: markus.raschke@colorado.edu
Y. Wang, M. Hu
Terahertz Research Center
School of Electronic Science and Engineering
University of Electronic Science and Technology of China
Chengdu 610054, China
N. Nookala
Department of Electrical and Computer Engineering
The University of Texas at Austin
Austin, TX 78712, USA
J. F. Klem, I. Brener
Sandia National Laboratories
Albuquerque, NM 87185, USA
S. R. Turner
Advanced Light Source
Lawrence Berkeley National Laboratory
Berkeley, CA 94720, USA
E. A. Muller
Department of Chemistry
Colgate University
13 Oak Drive, Hamilton, NY 13346, USA
E-mail: emuller@colgate.edu
A. Belyanin
Department of Physics and Astronomy
Texas A&M University
College Station, TX 77843, USA
E-mail: belyanin@physics.tamu.edu
M. A. Belkin
Walter Schottky Institute
Technical University of Munich
85748 Garching, Germany
E-mail: mikhail.belkin@wsi.tum.de

The ORCID identification number(s) for the author(s) of this article can be found under https://doi.org/10.1002/lpor.202301148

DOI: 10.1002/lpor.202301148

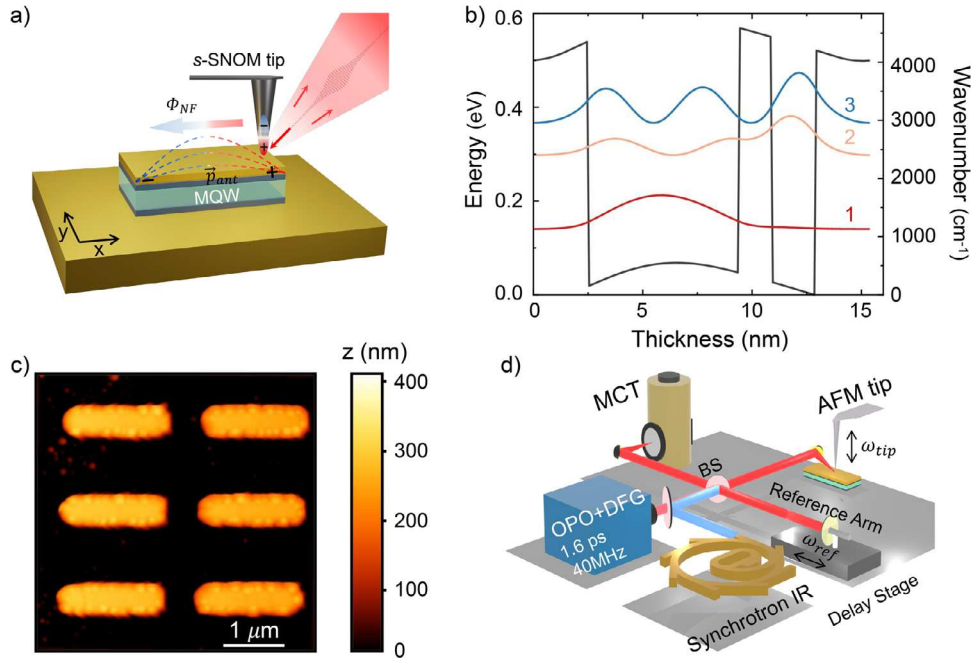

Figure 1. Antenna-MQW heterostructure nano-imaging a) Nano-imaging of the antenna-MQW heterostructure, with tip-enhanced near-field interference controlling the excitation of the antenna-MQW cavity mode and the saturation of the intersubband transition. b) 1D potential energy diagram of the MQW heterostructure with an intersubband transition between $|1\rangle$ and $|2\rangle$ of $\tilde{\nu}^0_{qw} = 1315\ \mathrm{cm}^{-1}$. c) AFM topography of the antenna-MQW array for the case of antenna length $l_{ant} = 1.60\ \mu\mathrm{m}$. d) IR *s*-SNOM with the optical layout for broadband synchrotron (weak field) and picosecond OPO/DFG (strong field) nano-spectroscopic imaging and control of strong coupling.

small as $10^{-6}(\frac{\lambda}{n})^3$, with wavelength λ and refractive index n of the local environment, have drawn attention as new cavity quantum electrodynamics (cQED) platforms.[17–20] In particular, room temperature vibrational strong coupling of molecular vibrations has been observed in both surface phonon polariton and surface plasmon polariton-based nano-resonators.[8,21,22]

Here, the nano-scale mode volume can overcome the low Q-factor and dissipation losses of an open cavity, and strong coupling was demonstrated even at room temperature.[3,8,18,19,23–25]

Achieving strong coupling in quantum systems with large, controllable transition dipole moments has remained challenging across the visible to IR spectral regions. In the visible, quantum dots, color centers, or molecules exhibit large transition dipole moments, allowing for electronic strong coupling (ESC) even for single emitters.[11,12,24] In contrast, reaching the strong coupling regime in the IR has been limited to macroscopic ensembles due to weaker transition dipole moments and similarly lossy IR nano-cavities compared to the visible.

Nevertheless, IR vibrational strong coupling (VSC) with molecular vibrations in conventional high Q microcavities has attracted much interest for its potential to modify ground state chemical reactivity.[13–16,18,22,26,27] Similarly, using IR plasmonic antenna cavities allows for probing large Purcell enhancement of molecular vibrations and resolving intramolecular relaxation dynamics.[28,29] However, due to weak vibrational transitions and their low energies corresponding to long resonant wavelengths, VSC has rarely been achieved with IR nano-plasmonic resonators, except when coupled to surface plasmon polaritons as collective excitations.[3,4]

Multi-quantum-well (MQW) heterostructures with engineered electronic transitions offer a promising new route toward mid-infrared strong coupling. Strong coupling of MQW-coupled IR-antenna arrays has been established with strongly dipole-active electronic intersubband (ISB) transitions.[23,25,30–32] Nonlinear saturable absorption and ultrafast switching in strong coupling have also been demonstrated with antenna-array metasurfaces combined with patterned MQWs.[23,25,33–35] Antenna-MQW systems combining ISB transitions and a plasmonic cavity offer a combination of strong optical nonlinearity, ultrafast response, the possibility of electric tuning, and chip-scale integration. As one example, fast modulation of the reflectivity of MIR antenna-MQW systems has received significant attention recently due to the potential use of these systems as amplitude[36] and phase[37] modulators for free-space optical data links in the long-wave infrared (8–14 μm)[38] atmospheric transparency windows.[39]

Similarly, we have previously proposed the possibility of phase-dependent nonlinear control of molecular vibrations, which could open routes to quantum optical processing and coherent control of ground state chemical reaction dynamics.[40,41]

Here, in order to achieve nano-scale coherent control of strong coupling, we use a metallic scanning probe tip to both image and perturb the strongly coupled antenna-MQW system through tip-induced local interference of the antenna field, as illustrated in **Figure 1a**. We show that a non-resonant tip near-field coupling to the antenna increases optical confinement beyond that of the antenna alone, providing for nano-optical control of IR strong coupling. Further, the antenna-enhanced near-field interaction lowers the field threshold for saturable absorption.[42] By changing

the excitation from weakly perturbing ultra-broadband low spectral irradiance synchrotron radiation to narrowband picosecond pulsed laser excitation with strong fields, we control the transition between weak and strong coupling through modifications of coupling strength between the antenna and MQW resulting from intersubband saturation.

Scanning the nanotip position along the antenna provides for spatial control of local constructive and destructive near-field interference between the far-field excited resonant antenna dipole field and a non-resonant tip-enhanced apex field (Figure 1a). This tunes the coupling strength g_{aq} from 73 (strong coupling) to 24 cm^{-1} (weak coupling) across the antenna-MQW heterostructure through the local field-dependent saturable absorption as described using an empirical coupled harmonic oscillator model. We then apply a quantum-mechanical density-matrix description of the MQW system based on the design parameters of the antenna-MQW heterostructure, including the saturation effects by the antenna field and local external tip interference as the only free parameters. The results establish the nano-optical analog of electromagnetically induced scattering (EIS)[41,43,44] through the phase-controlled interference between the nanotip and antenna for near-field excitation of a hybrid antenna-MQW system in the strong coupling regime.

2. Experimental Section

The antenna-MQW heterostructures consisted of IR-resonant gold dipole antennas, fabricated on top of a correspondingly patterned $In_{0.53}Ga_{0.47}As/Al_{0.48}In_{0.52}As$ MQW layer,[35] which was grown on an InP substrate using molecular beam epitaxy. The MQW stack consisted of 26 repetitions of the structure shown in Figure 1b with layer sequence 2.5/6.2/1.4/2.4/2.5 (in nm), where the first, third, and fifth layers represented the $Al_{0.48}In_{0.52}As$ barriers. The first 1.5 nm of the first 2.5 nm barrier and the last 1.5 nm of the last 2.5 nm barrier were nominally n-doped to $7.3 \times 10^{18} cm^{-3}$. The computed eigenvalues and probability densities in a single period of the MQW stack are shown in Figure 1b. The out-of-plane intersubband transition dipole moment of the MQW facilitates coupling to the antenna near-field. The absorption measurements[35] allowed to estimate the average electron density to be 8.3×10^{17} cm^{-3}, indicating that only ≈60% of the nominal doping in the barriers were activated.

Optical antenna arrays of varying lengths were designed as half-wavelength antennas and fabricated as 10 nm of Ti followed by 100 nm of Au using electron-beam lithography. The antenna length l_{ant} of each array varied from 1.23 to 1.98 μm. Figure 1c shows an atomic force microscopy (AFM) height image of a section of the antenna-MQW array, with uniform antenna dimensions and spacing observed across each array. By Fourier transform infrared (FTIR) micro-spectroscopy (Thermo Nicolet Continuum microscope, linked to a Nexus 670 FTIR spectrometer), spectra were measured in reflectance mode with 4 cm^{-1} spectral resolution from arrays of antenna-MQW.

The antenna-MQW strong coupling was then imaged and manipulated using a metallic AFM tip (Pt/Ir coated, ARROW-NCPt-50, NANO World, tapping at frequency 250kHz) in IR *s*-SNOM (Figure 1d). Incident light was polarized parallel to the tip with the incident *k*-vector along the antenna axis. For low-power excitation, synchrotron infrared nano-spectroscopy (SINS) (Beamline 5.4, Advanced Light Source, neaSCOPE, Neaspec GmbH)[45] was used with the spectral range of 700–5000 cm^{-1} and low average power (≤300 mW) at a spectral irradiance "≤10 $W/cm^2/cm^{-1}$". SINS nano-FTIR near-field spectroscopy was performed as established previously with lock-in demodulation at the second harmonic of the tip tapping frequency, which provides adequate near-field contrast[46] (see Supporting Information for details), and heterodyne interferometric detection of the tip-scattered near-field signal.[45] The Fourier transform of the asymmetric interferometer then provided the complex valued near-field signal as real Re_{NF} and imaginary Im_{NF}, or amplitude A_{NF} and phase ϕ_{NF}.

For high optical power excitation, a narrowband picosecond optical parametric oscillator (OPO) and difference-frequency generation (DFG) (Carmina, APE, repetition rate 40MHz) were used, with pulse duration ≈ 1.6ps, tuning from 930 to 1530 cm^{-1}, with spectral bandwidth ≈ 20 cm^{-1}. The IR pulses after passing a ZnSe beam splitter were focused onto the AFM tip (Pt/Ir coated, ARROW-NCPt-50, NANO World, tapping at frequency 250 kHz) by an off-axis parabolic mirror (OAP, focal length = 11 mm, NA ≈ 0.46), with a fluence of ≈400 $kWcm^{-2}$. Phase-resolved nano-imaging was performed for each wavelength using pseudo-heterodyne detection[47] based on an IR *s*-SNOM (neaSCOPE, Neaspec GmbH), where the tip-scattered near-field signal was combined with the reference field phase modulated by a mirror vibrating at 307 Hz. The signal was detected with a mercury cadmium telluride detector (MCT, KV104-0.5-A-1-SMA, KOLMAR Technologies), and then sideband demodulated using an integrated lock-in amplifier, at the sum of the second-harmonic of the tip tapping frequency and the mirror vibrating frequency. All spectra were normalized against either gold regions several tens of nanometers away from the antenna or non-resonant gold regions several millimeters away from the antenna. Similar spectra was observed in both normalization procedures, and it was concluded that the potential indirect illumination artifacts were eliminated.[48]

3. Results

We first characterize the unperturbed antenna-MQW coupling as a function of antenna resonance in each array through far-field micro-FTIR spectroscopy. **Figure 2a** shows a series of reflectance spectra measured with corresponding fits to the coupled oscillator model. Figure 2b shows the evolution of the two polaritonic modes in the strong coupling, with $\tilde{\nu}^0_{qw} = 1315$ cm^{-1}, and varying antenna length l_{ant} from 1.23 μm with fit values $\tilde{\nu}^0_{ant} = 1843$ cm^{-1} and $\gamma^0_{ant} = 110$ cm^{-1}, to 1.98 μm with fit values $\tilde{\nu}^0_{ant} = 1016$ cm^{-1} and $\gamma^0_{ant} = 110$ cm^{-1}. The derived coupling strength of $g_{aq} = 140$ cm^{-1} with splitting $2g_{aq} = 280$ cm^{-1} meets the threshold for strong coupling of the antenna-MQW hybrid system, that a local minimum appears between two resonances, and that $2\ g_{aq} \geq \tilde{\nu}_{ant} + \tilde{\nu}_{qw}$.[49,50]

In IR *s*-SNOM, the metallic AFM tip provides a controllable second optical excitation pathway through the near-field tip-antenna interference in addition to the direct excitation of the antenna by the incident IR beam. We scan the tip along the length of an antenna under synchrotron IR illumination, in order to control the near-field interference between the antenna-MQW and the metallic tip fields.

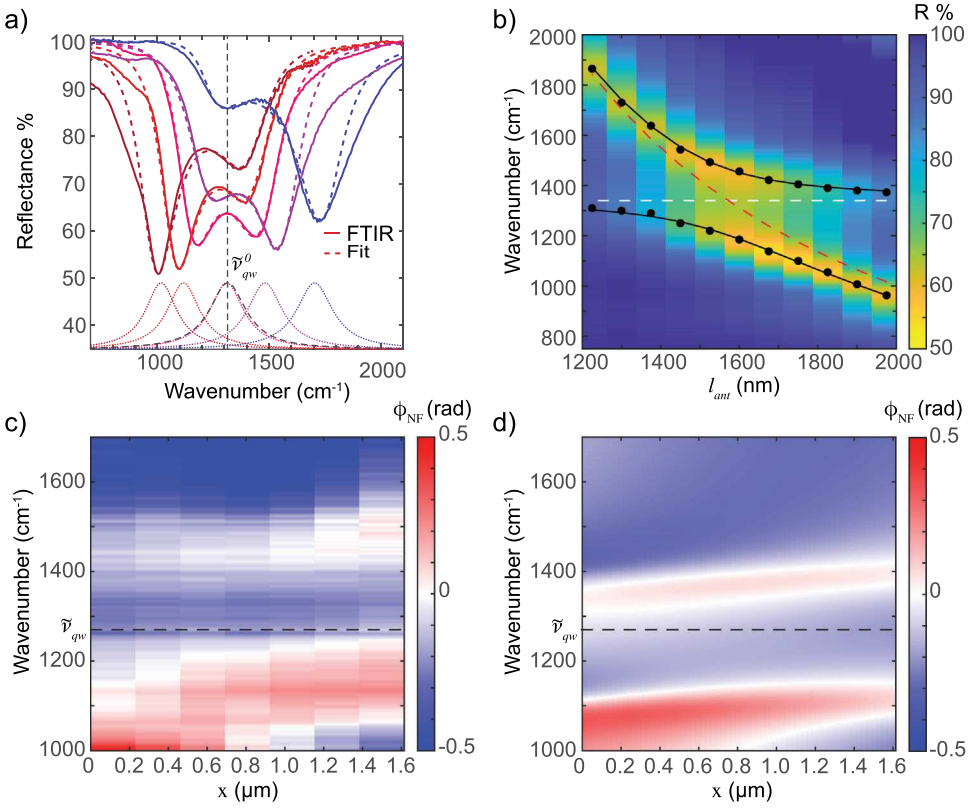

Figure 2. Antenna-MQW IR strong coupling a) Micro-FTIR reflectance spectra (solid lines) with fits to the coupled oscillator model (dashed lines) for a subset of antennas with lengths l_{ant} varying from 1.23 μm (blue) to 1.98 μm (brown). The MQW ISB frequency ($\tilde{\nu}^0_{qw}$ = 1315 cm^{-1}) is indicated by the vertical dashed line. b) Derived tuning curves (black circles) of the antenna-MQW hybrid system with fit (black lines) demonstrating the avoided crossing. MQW frequency (white dashed line) and the length dependent resonance of the antenna (red dashed line) in the absence of coupling are overlaid. Fits are overlaid on a false-color plot of the spectral response for each antenna-MQW array. c) Corresponding SINS phase spectra for a line scan along the length of the antenna $\tilde{\nu}_{ant}$ = 1240 cm^{-1}, with the fit value of $\tilde{\nu}_{qw}$ = 1260 cm^{-1} in dashed black. d) Modeled SINS phase spectra based on the classical coupled-harmonic-oscillator model as a function of tip position with retardation-induced modification of the relative optical driving field for the tip and antenna.

Figure 2c shows the spectrally resolved line scan as near-field phase spectra ϕ_{NF}. The quantum well transition fit value ($\tilde{\nu}_{qw}$ = 1260 cm^{-1}, black dashed line) is near-resonant with the antenna ($\tilde{\nu}_{ant}$ = 1240 cm^{-1}, l_{ant} = 1.60 μm) chosen for this experiment, both of which are red-shifted from the far-field value $\tilde{\nu}^0_{qw}$ (for details see Supporting Information). As expected, we again observe two well-separated peaks in ϕ_{NF} due to strong coupling.

Although the resonances of the quantum well and antenna are fixed, the addition of the metallic nanotip perturbs the overall spectral response. As the tip scans along the antenna, both the lower and upper polariton peaks appear to blue shift, associated with a change in the dispersive line shape. Modeled spectra, shown in Figure 2d (for details see below), reproduce the evolving dispersive line shape and simultaneous blue-shift of the two modes.

Next, we perform IR *s*-SNOM under high optical intensity illumination with narrowband ps IR radiation. We set the laser fluence to ≈400 kWcm^{-2}, which is near the MQW saturation condition when illuminated in the far-field.[35] We acquire pseudo-heterodyne near-field spatio-spectral images for each frequency from 930 to 1530 cm^{-1}, in steps of 50 cm^{-1}, average the phase ϕ_{NF} over the width of the antenna, and thus derive spectra as a function of the tip position along the length of the antenna.

Figure 3a–c shows images of a l_{ant} = 1.60 μm antenna-MQW simultaneously measured as a) AFM topography, b) near-field amplitude A_{NF}, and c) near-field phase ϕ_{NF} with incident light tuned to 1330 cm^{-1}. We observe the expected dipole pattern of the antenna in ϕ_{NF} with π phase change between the two poles of the antenna. Figure 3d shows six representative ϕ_{NF} spectra measured as a function of tip positions across the antenna, with the location of the tip for each measured spectrum indicated as points 1–6 in Figure 3c. With the tip positioned on the left side of the antenna (position 1–3), we observe the two polariton peaks $\tilde{\nu}_+$ and $\tilde{\nu}_-$ in ϕ_{NF} due to a reduced field intensity caused by destructive interference between the tip and antenna field, although the splitting is reduced compared to the spectra measured under low- intensity illumination with the synchrotron source in SINS. Scanning the tip to the opposite terminal of the antenna (position 4–6), the two polariton peaks merge into a single peak because of the constructive interference with enhanced field giving rise to saturation. In addition to an evolution of the dispersive line shape, a change in sign of the overall spectrum is observed.

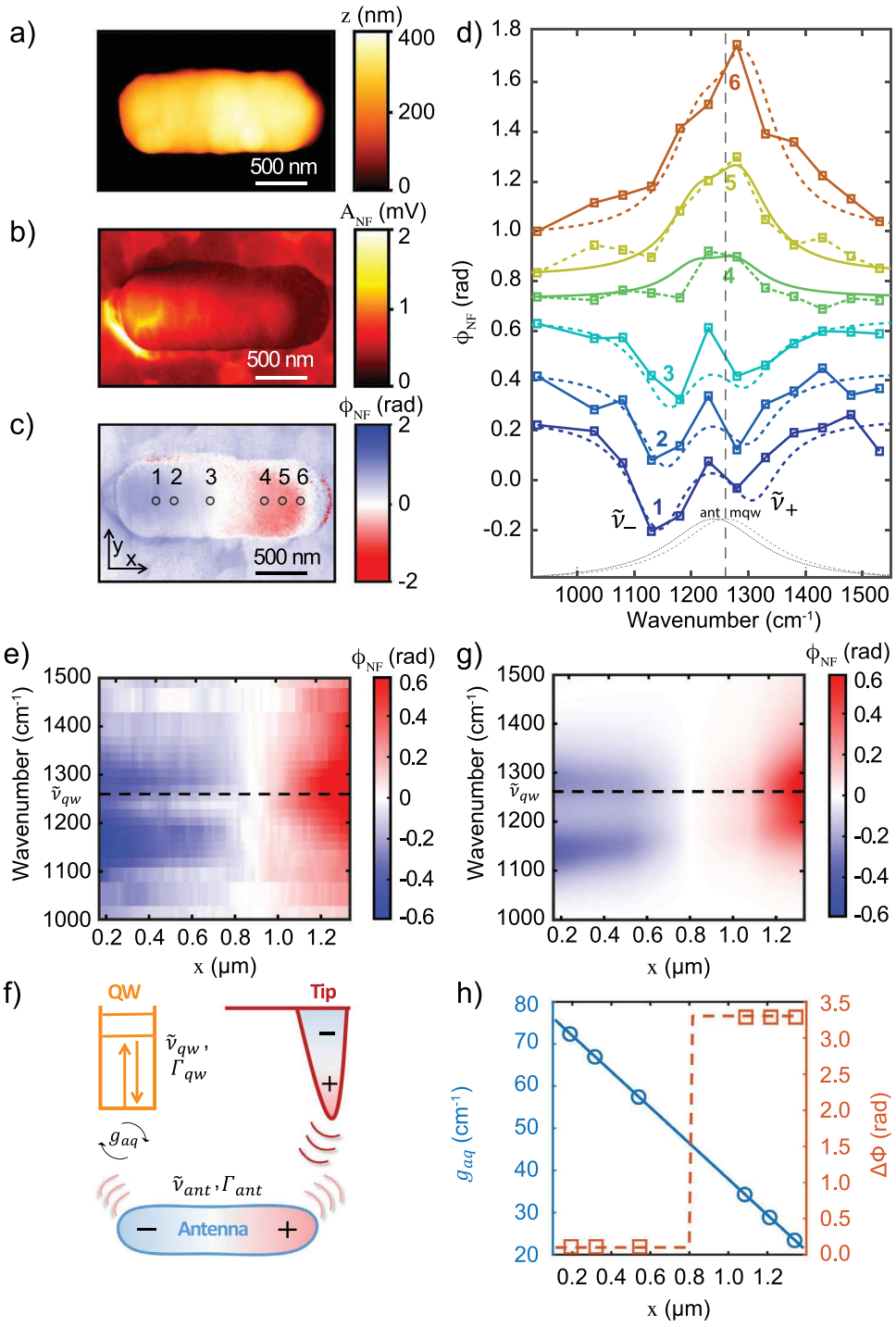

Figure 3. Tip-enhanced control of antenna-MQW strong coupling IR *s*-SNOM nano-imaging of a single antenna-MQW structure, a) topography, b) amplitude A_{NF} with a laser tuned to 1330 cm^{-1}, and c) corresponding phase ϕ_{NF}. d) Spectra of ϕ_{NF} measured as a function of tip positions across the antenna (open circles in c), with MQW ISB transition frequency $\tilde{\nu}_{qw}$ = 1260 cm^{-1} (black dashed). e) Surface plot of the ϕ_{NF} spectra measured as a function of tip position X along the antenna in steps of 15 nm, with MQW ISB transition frequency $\tilde{\nu}_{qw}$ = 1260 cm^{-1} (black dashed). f) Schematic of coupling between antenna, MQW, and AFM tip. The non-resonant tip-antenna interaction modifies the local driving field through spatial antenna phase-dependent near-field interference. g) Surface plot of modeled ϕ_{NF} spectra as a function of tip position X for the $\Delta\phi$ and g_{aq} parameters shown in (h). h) Modeled coupling strength g_{aq} and $\Delta\phi$ as a function of tip position X along the antenna length.

4. Theory

4.1. Coupled Harmonic Oscillator Modeling

In order to describe the spectral response dependence on illumination intensity and nanotip position, we implement an empirical classical coupled oscillator model as illustrated in Figure 3f. We begin with the equations of motion for the charge displacement x in the antenna, quantum well, and metallic nanotip, respectively. For the antenna and quantum well, we include harmonic restoring force constants k and damping rate γ, while we assume a Drude response from the metallic tip. Including empirical coupling constants κ_{ij}, the equations of motion become

$$\ddot{x}_{tip} + 2\gamma_{tip}\dot{x}_{tip} + \kappa_{ta}(x_{tip} - x_{ant}) + \kappa_{tq}(x_{tip} - x_{qw}) = eE_{tip}(t) \quad (1)$$

$$\ddot{x}_{ant} + k_{ant}x_{ant} + 2\gamma_{ant}\dot{x}_{ant} + \kappa_{ta}(x_{ant} - x_{tip}) + \kappa_{aq}(x_{ant} - x_{qw}) = eE_{ant}(t) \quad (2)$$

$$\ddot{x}_{qw} + k_{qw}x_{qw} + 2\gamma_{qw}\dot{x}_{qw} + \kappa_{aq}(x_{qw} - x_{ant}) + \kappa_{tq}(x_{qw} - x_{tip}) = 0 \quad (3)$$

with optical driving fields $E_i(t)$ for antenna and nanotip. We assume the quantum well is driven by tip and antenna interaction only, neglecting direct far-field excitation.

We first solve for the steady-state solutions of the coupled antenna and quantum well in a two-oscillator model. In the case of small damping, this yields the well-known polariton splitting of the hybridized modes given by

$$\omega_{\pm}^2 = \frac{1}{2}\left[\omega_{ant}^2 + \omega_{qw}^2 \pm \sqrt{(\omega_{ant}^2 - \omega_{qw}^2)^2 + 4g_{aq}^2\omega_{ant}\omega_{qw}}\right] \quad (4)$$

On resonance, the Rabi splitting is given by $\Omega = 2g_{aq} = \frac{1}{2\pi c}\frac{\kappa_{aq}}{\sqrt{\omega_{ant}\omega_{qw}}}$, with $\omega_{qw} = \sqrt{k_{qw} + \kappa_{aq}}$ and $\omega_{ant} = \sqrt{k_{ant} + \kappa_{aq}}$.

Including the non-resonant IR *s*-SNOM tip, we then solve the system of three coupled equations for the induced polarization of the nanotip $P_{tip} = e \cdot x_{tip}$, which effectively represents the measured *s*-SNOM signal (see Supporting Information for details). We first apply this model to the low optical intensity scenario with synchrotron radiation, with results shown in Figure 2d for the quantum well with $\tilde{\nu}_{qw} = 1260$ cm^{-1} and the antenna $\tilde{\nu}_{ant} = 1240$ cm^{-1}, with damping rates $\gamma_{qw} = 110$ cm^{-1} and $\gamma_{ant} = 110$ cm^{-1}, respectively, and coupling strength $g_{aq} = (140 \pm 10)$ cm^{-1}. Values are expressed in wavenumbers in accordance with spectroscopic convention and easier comparison with the experiment. We represent the metallic tip using the Drude–Lorentz model by setting the restoring force constant to zero and typical damping rate to 150 cm^{-1} ($\tau_D \approx 30$ fs) determined by the electron scattering time. We use free parameters for the phase and amplitude of the driving field for the tip relative to the driving field for the antenna.

Figure 2d shows the spectral evolution of the antenna-MQW system as a function of the tip position X based on a global fit. In this model, changes in the spectral response with tip position are calculated assuming a lowest-order linear dependence on tip position, implemented as a global fit. We find that the overall change in dispersion and the appearance of a blue shift in the peaks of both the upper and lower polaritonic modes is well reproduced by varying the phase $\Delta\phi$ and amplitude of the optical driving field for the optical antenna relative to the nanotip $E_{tip} = E_{ant}e^{i\phi}$. That phase $\Delta\phi$ increases by π radians, changing linearly with the nanotip position X, while all other physical parameters remain constant including the coupling strength $g_{aq} = 140$ cm^{-1}, which is identical to the value we observe in micro-FTIR, i.e., in the absence of the tip (Figure 2a,b).

We then apply the model to the case of high optical intensity with fixed parameters (see details in Supporting Information) for antenna and MQW resonance. We assume a linear dependence of antenna-MQW coupling strength g_{aq} on the tip position based on the approximate linear variation of the driving field with tip position along the antenna for the global fit, as shown in Figure 3d (dashed lines).

Figure 3h shows the resulting variation of g_{aq} decreasing from $g_{aq} = 73$ cm^{-1} to $g_{aq} = 24$ cm^{-1} as a function of tip position along the antenna. Note that the largest coupling strength value of $g_{aq} = 73$ cm^{-1} with the tip at position 1 is lower compared to the value measured under low optical illumination conditions. With the tip positioned on the opposite antenna terminal (position 6) with $g_{aq} = 24$ cm^{-1}, the system is in a weak coupling regime. Figure 3h also shows that the relative phase $\Delta\phi$ between IR driving fields of the antenna and tip changes by π radians. The amplitude of the driving field is greatest at the two ends of the antenna, reflecting the dipolar response of a half-wavelength antenna. We show the comparison between experimentally measured and modeled ϕ_{NF} in Figure 3f,g as well as the corresponding experimental and modeled A_{NF} in Figure S4a,b (Supporting Information). The overall change in dispersive line shape and sign of the ϕ_{NF} spectra, as well as the decrease and disappearance of splitting between upper and lower polaritons are well reproduced by varying the IR driving field for the nanotip relative to the antenna in the model.

The observed collapse of hybrid mode splitting with nanotip position is only reproduced assuming a decrease in coupling strength g_{aq} between antenna and MQW. This supports the interpretation of a saturation-induced transition from strong to weak coupling when the coupling strength g_{aq} drops below the combined antenna and MQW loss rates.

Figure 4a illustrates the transition from weak to strong coupling, based on the parameters as determined by the experiment above. We model an increase in g_{aq} increasing from 20 to 100 cm^{-1} with constant $\Delta\phi = 0.5$ rad, $\tilde{\nu}_{ant} = 1240$ cm^{-1}, and $\tilde{\nu}_{qw} = 1260$cm^{-1}. Modeled spectra illustrate the appearance of the two polaritonic eigenstates for $g_{aq} \gtrsim 75$ cm^{-1}. Figure 4b shows spectra for selected values of $\Delta\phi$ (–2 to 3 rad) for fixed $g_{aq} = 75$ cm^{-1}, illustrating the changes in dispersive line shape and simultaneous spectral shift of both modes. Only by varying both $\Delta\phi$, and g_{aq} we are able to model the simultaneous collapse of the polariton bands into a single peak and the dispersion dependence on tip position that were both observed in the high intensity experiment. These results precisely demonstrate the localized modification of tip-induced phase retardation in cavity excitation pathways.

4.2. Coupled Maxwell and Density-Matrix Equations

We now interpret the experimental results in terms of the model which describes the dynamics of the classical electric field of the antenna mode coupled with the quantum-mechanical density matrix description of subband populations and intersubband

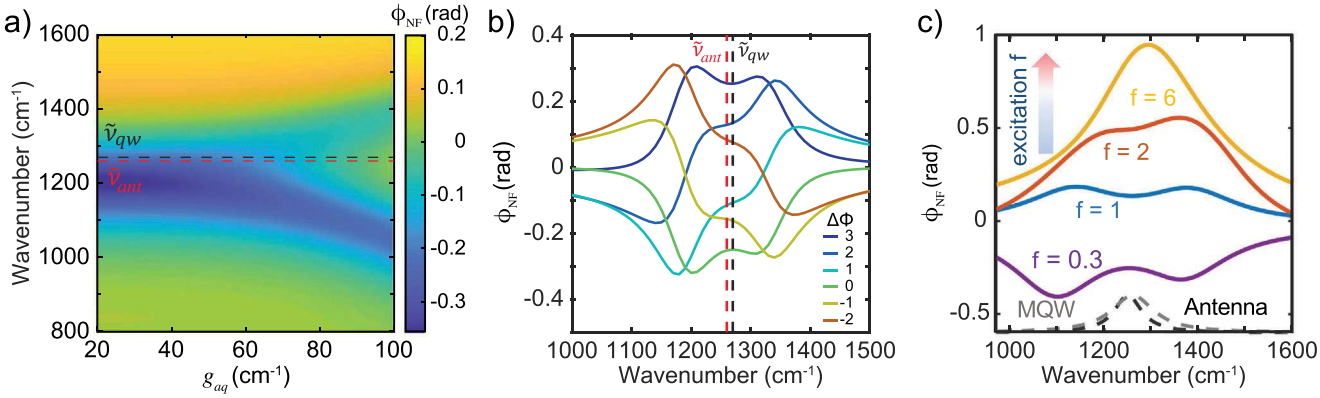

Figure 4. Classical and quantum model of antenna-MQW strong coupling a) Spectral evolution based on coupled-oscillator modeling as a function of g_{aq}, with the asymmetric splitting of the two polaritonic states, with $\Delta\phi = 0.5$ rad, $\tilde{\nu}_{ant} = 1240\ \mathrm{cm}^{-1}$ and $\tilde{\nu}_{qw} = 1260\ \mathrm{cm}^{-1}$. b) Spectra with $g_{aq} = 75\ \mathrm{cm}^{-1}$, varying the $\Delta\phi$ from 3 to –2 rad. c) The spectra of ϕ_{NF} based on density matrix formalism for four different excitation field amplitudes f and phases.

polarization in the semiconductor MQW structure used in the experiment. This approach is based on the designed parameters of QW band structure: doping concentration, transition frequencies, realistic values of the intersubband dipole matrix element, intersubband transition broadening, and upper subband lifetime. The density matrix approach correctly describes the coupling of light to ISB transitions and the saturation effects of the strong electric field of the antenna with a minimum amount of free parameters and complements the classical description. In fact, the only arbitrary fitting parameters in the model are the amplitude and relative phase of the external tip excitation with respect to the antenna mode.

The coupled cavity field and density-matrix equations can be written as[51]

$$\frac{d^2e}{dt^2} + \frac{2}{T_E}\frac{de}{dt} + \omega_{ant}^2 e = -\frac{4\pi\Gamma}{\epsilon}\frac{d^2p}{dt^2} + f(t) \tag{5}$$

$$\frac{d^2p}{dt^2} + \frac{2}{T_2}\frac{dp}{dt} + \omega_{qw}^2 p = \frac{2d^2\omega_{qw}(\Delta n)e}{\hbar} \tag{6}$$

$$\frac{d\Delta n}{dt} + \frac{\Delta n - \Delta n_0}{T_1} = -\frac{2e}{\hbar\omega_{qw}}\frac{dp}{dt} \tag{7}$$

Here, $e(t)\vec{\mathcal{E}}(\vec{r})$ is the electric field of the electromagnetic mode in an antenna cavity with effective dielectric constant ϵ and field decay time T_E; $f(t)$ is an external excitation, mostly due to the tip; ω_{ant} is the mode frequency in the cold cavity, i.e., without the resonant contribution from intersubband transitions; ω_{qw} is the transition frequency between subbands 1 and 2 neglecting nonparabolicity which is insignificant for this structure as compared to the homogeneous broadening; $p(t) = \mathrm{Tr}[\hat{d}\hat{\rho}]/V$ is the averaged (traced with density matrix $\hat{\rho}$) intersubband polarization due to transitions between subbands 1 and 2 only, and assuming that time and space dependence of the polarization can be factorized; $\Gamma \approx 0.8$ is a normalized overlap integral of the spatial distribution $\vec{\mathcal{E}}(\vec{r})$ of the cavity field with the spatial distribution of the polarization within the cavity volume; $\Delta n = n_1 - n_2$ is the volume density of the population difference between lower and upper subbands (in 1 cm^{-3}); $\Delta n_0 \approx n_1$ is the same population difference in equilibrium in the absence of any excitation, when it is equal to the ground state subband population density neglecting thermal excitation to upper subbands; d is the magnitude of the intersubband dipole moment, which is oriented along z-direction (the QW growth direction); T_1 and T_2 are relaxation times of the population difference and polarization. In writing Equations (5–7) we neglected many-body Coulomb effects since they are insignificant at our moderate level of doping.

For weak excitation $\Delta n \approx \Delta n_0$, Equations (5 and 6) are linear. One can take the Fourier transform of these equations assuming $\propto \exp(-i\omega t)$ dependence and solve the algebraic equation for eigen-frequencies and the equation for the scattered field spectrum $\propto E(\omega)$. For strong excitation one needs to integrate the nonlinear set of equations, usually numerically.

The above equations can be further simplified in the rotating-wave approximation for slowly varying complex amplitudes of the electric field $E(t)$, polarization $P(t)$, and the excitation term $F(t)$, as long as all frequencies of interest are close to each other and all coupling strengths are small as compared to ω_{qw} and ω_{ant}. Using $e = \frac{1}{2}E(t)\exp(-i\omega t) + \text{c.c.}$, $p = \frac{1}{2}P(t)\exp(-i\omega t) + \text{c.c.}$, and $f = \frac{1}{2}\omega_{ant}F(t)\exp(-i\omega t) + \text{c.c.}$, one can obtain

$$\frac{dE}{dt} + \left(\frac{1}{T_E} + i(\omega_{ant} - \omega)\right)E = \frac{2\pi i\omega_{ant}\Gamma}{\epsilon}P + F \tag{8}$$

$$\frac{dP}{dt} + \left(\frac{1}{T_2} + i(\omega_{qw} - \omega)\right)P = \frac{id^2\Delta nE}{\hbar} \tag{9}$$

$$\frac{d\Delta n}{dt} + \frac{\Delta n - \Delta n_0}{T_1} = -\mathrm{Im}(E^*P)/2\hbar \tag{10}$$

For weak excitation and in the absence of any losses one obtains the usual anticrossing at $\omega_{ant} = \omega_{qw}$, with splitting by $\pm\omega_c$ at resonance. Here

$$\omega_c^2 = \frac{8\pi\Gamma d^2\omega_{qw}\Delta n_0}{\hbar\epsilon} \tag{11}$$

is a square of the so-called cooperative frequency which measures the strength of the coupling between the two-level system and the electric field.

If the excitation pulse is much longer than all relaxation and dynamic times in the system (which is true in our case), we

can solve the equations analytically in steady-state. We drop time derivatives in Equations (8–10), eliminate the polarization and populations, and solve for the complex amplitude of the antenna field E,

$$\left(\alpha - i(\omega - \omega_{ant})\right)E + \frac{\omega_c^2}{4\gamma_{qw}^2}\frac{(\gamma_{qw} + i(\omega - \omega_{qw}))E}{1 + \frac{(\omega_{qw} - \omega)^2}{\gamma_{qw}^2} + \frac{|E|^2}{E_{sat}^2}} = F \tag{12}$$

where $\alpha = \frac{1}{T_E}$ and $\gamma_{qw} = \frac{1}{T_2}$. The saturation field squared is defined as

$$E_{sat}^2 = \frac{2\hbar^2\gamma_{qw}}{T_1 d^2} \tag{13}$$

Figure 4c shows the spectral phase of the antenna field normalized by the saturation field for four different excitation field amplitudes and phases, and for the same QW and antenna resonant frequencies and damping rates as used for the coupled harmonic oscillator model shown in Figure 3. The variation of the excitation amplitude, defined as $f = |F|/(\gamma_{qw}E_{sat})$, simulates the variation of the tip position from 1 to 6 in Figure 3a with excitation phase flipping by π radians between the bottom curve and the top curves. These results reproduce the effect of saturation of the population difference across the intersubband transition which switches the system from the strong to weak coupling regime (for parameters see Supporting Information).

5. Discussion

The results demonstrate nanotip near-field localized modification of IR electronic strong coupling between a single nano-antenna and a MQW ISB transition. Here, the IR nano-antennas, with their high spatial field confinement and reduced mode volume, act as plasmonic nanocavities giving rise to the observed IR ESC.[52] While plasmonic nanocavities exhibit higher loss rate and lower quality factor compared to phononic nanoresonators,[53,54] or Mie modes of dielectric nanoresonators,[25] they provide for high bandwidth and tunability.

Quantum-engineered MQW ISB transitions with large and controllable transition dipoles and ultrafast relaxation times offer mid-infrared strong light-matter interaction on ultrafast timescales at room temperature.[35,55] The MQW ISB transition dipole ($d/e \approx$ 1.76 nm in this work) is about two orders of magnitude larger than IR active molecular vibrations ($d/e \approx 2.08 \times 10^{-2}$ nm for C=O carbonyl stretch modes,[56] $d/e \approx 0.705 \times 10^{-2}$ nm for C—H stretch modes[57]). This enables the MQW system to readily reach the strong coupling regime when coupled to a plasmonic cavity despite the relatively low doping density ($\Delta n_0 \approx 10^{18}$ cm^{-3} in this work), compared to the number of atoms per volume in bulk PMMA ($n \approx 10^{22}$ cm^{-3}). However, the higher density of oscillators in molecular films can compensate for their weaker transition dipole. One would thus expect similarly large coupling strength in IR antennas coupled to, e.g., a thin PMMA film, when sandwiched between metallic ground plane and antenna. This would provide a perspective to achieve vibrational strong coupling and control in nanoscale molecular ensembles.

With our antenna-MQW heterostructure, we further control the light-matter interactions through nanotip controlled local interference based on saturation of the quantum well state. Using nanotip positioning to induce constructive and destructive excitation interference at the representative antenna terminals, and the associated transition from weak to strong coupling, demonstrates dynamic local control of strong coupling. Metallic tips have been shown to manipulate coherent coupling interactions between plasmonic and polaritonic materials and molecular transitions,[22,53,54,58] which is achieved through interference between different excitation pathways in optical cavities.[4,29,41] Compared with far-field low-resolution excitation,[25,35] the deep sub-wavelength field confinement of the nanotip offers a platform for coherent phase manipulation in the near-field through spatially dependent coupling and local interference, which provides efficient nano-optical control of infrared electronic strong coupling.

In previous studies,[53,54] the antenna coupling to molecular vibrations is modeled by a classical two-oscillator model, where the tip is assumed to only passively interact to provide for the tip-scattered signal emissions, but not manipulate the coupling interaction itself. However, in our case, taking advantage of the phase retardation between the metallic tip and antenna, the tip provides for the active local modification to the excitation pathways of the antenna in two ways: Under weak excitation, the antenna and MQW are strongly coupled with a constant coupling strength of g_{aq} = 140 cm^{-1} and remain unperturbed by the tip interaction. However, the tip modifies the phase of the excitation field, giving rise to changes in spectral lineshape of the antenna-MQW signal. Under strong excitation, the tip-induced interference pathways in addition change the local driving field strength giving rise to the saturation induced modification of coupling strength g_{aq} from 73 to 24 cm^{-1}.

In previous work,[41] we demonstrated phase-controlled excitation using a similar non-resonant tip to modify a hybrid state of an optical antenna coupled to molecular vibrational modes, and we modeled the scattered spectrum through a classical model for electromagnetically induced scattering (EIS). Several studies have investigated the saturation of cavity-coupled vibrational modes in weakly coupled systems, including observation of decreased Rabi coupling in pump-probe measurements.[59] Vibrational modes have also been investigated as a route toward control of the Rabi splitting through saturation,[60] including measurement of strongly coupled $W(CO)_6$.[61] Although the anharmonicity of the bond could be expected to sufficiently shift the $\nu_1 \rightarrow \nu_2$ to cause a saturation effect with a high population of $\nu = 1$, it was found that this was not possible under practical concentrations. In this work, we utilize the sufficiently anharmonic MQW intersubband transition with its large transition dipole to demonstrate control of Rabi splitting in a strongly coupled system by varying the position of the tip above the antenna.

Our combined experimental and theoretical results demonstrate a robust and generalizable route toward dynamic control of strong coupling with a saturable quantum transition, also implying a new regime for exploring the coherent and tunable IR electronic strong coupling between quantum-engineered large ISB transition dipoles and open system nano-cavity plasmonic resonances at room temperature. The coupling between the MQW ISB transition and the local electromagnetic field

in the plasmonic nano-cavity is controlled by ground state depletion, which could be applicable in quantum state control and ultrafast quantum information processing at mid-infrared frequencies.[23,25,35,52] We have demonstrated the potential for localized and dynamic modification of quantum states and excitation pathways via a non-resonant nanotip. Possible applications include nano-scale sensing, single-emitter femtosecond spectroscopy, and quantum information processing and computing, which highlights the potential for optical control of power limiters or saturable absorbers on the nano-scale.

Supporting Information

Supporting Information is available from the Wiley Online Library or from the author.

Acknowledgements

Y.W. and A.B. acknowledge support from the Air Force Office of Scientific Research grant no. FA9550- 21-1-0272 for nano-imaging and theory. S.C.J., S.R.T., and M.B.R. acknowledge support by the National Science Foundation (NSF) Science and Technology Center on Real-Time Functional Imaging (STROBE) under Grant DMR 1548924 for nano-IR instrument development. R.L.P. and M.B.R. acknowledge support from the National Science Foundation (NSF GrantNo. CHE2108009) for conceptualization and modeling. N.N. and M.A.B. acknowledge the support of the DARPA NASCENT program. Y.W. and M.H. acknowledge support from the National Key Research and Development Program (2020YFA0714001). The authors thank Richard Puro and Hans A. Bechtel for the SINS measurements at the Advanced Light Source at Lawrence Berkeley National Laboratory. The Advanced Light Source is supported by the Director, Office of Science, Office of Basic Energy Sciences, of the U.S. Department of Energy under contract No.DE-AC02-05CH11231. This work was supported in part by the U.S. Department of Energy, Office of Science, Office of Workforce Development for Teachers and Scientists (WDTS) under the Science Undergraduate Laboratory Internship (SULI) program.

For all the fabrication and far-field pre-characterization, the Sandia team acknowledges the support by the U.S. Department of Energy, Office of Basic Energy Sciences, Division of Materials Sciences and Engineering. Sandia National Laboratories is a multimission laboratory managed and operated by National Technology and Engineering Solutions of Sandia, LLC., a wholly owned subsidiary of Honeywell International, Inc., for the U.S. Department of Energy's National Nuclear Security Administration under contract DE-NA0003525. This paper describes objective technical results and analysis. Any subjective views or opinions that might be expressed in the paper do not necessarily represent the views of the U.S. Department of Energy or the United States Government.

This article has been authored by an employee of National Technology & Engineering Solutions of Sandia, LLC under Contract No. DE-NA0003525 with the U.S. Department of Energy (DOE). The employee owns all right, title and interest in and to the article and is solely responsible for its contents. The United States Government retains and the publisher, by accepting the article for publication, acknowledges that the United States Government retains a non-exclusive, paid-up, irrevocable, world-wide license to publish or reproduce the published form of this article or allow others to do so, for United States Government purposes. The DOE will provide public access to these results of federally sponsored research in accordance with the DOE Public Access Plan https://www.energy.gov/downloads/doe-public-access-plan.[IB1]

The authors also thank Roland Wilcken, Benjamin G. Whetten, and Sichong Ma for helpful discussions.

Conflict of Interest

The authors declare no conflict of interest.

Author Contributions

Y.W. and S.C.J. contributed equally to this work. S.C.J. and M.B.R. conceived and designed the experiments. Y.W. and S.C.J. conducted the measurements with guidance from M.B.R. and E.A.M.. Samples were fabricated by N.N., J.F.K., I.B., and M.A.B.. E.A.M., and A.B. developed modeling and theory. Y.W., E.A.M., A.B., and M.B.R. wrote the manuscript with the help of all authors.

Data Availability Statement

The data that support the findings of this study are available from the corresponding author upon reasonable request.

Keywords

IR spectroscopy, light-matter interaction, nano optics, quantum system, strong coupling

Received: November 7, 2023
Revised: June 8, 2024
Published online:

[1] O. Bitton, S. N. Gupta, G. Haran, *Nanophotonics* **2019**, *8*, 559.
[2] L. Novotny, *Am. J. Phys.* **2010**, *78*, 1199.
[3] F. J. Garcia-Vidal, C. Ciuti, T. W. Ebbesen, *Science* **2021**, *373*, eabd0336.
[4] J. F. Triana, M. Arias, J. Nishida, E. A. Muller, R. Wilcken, S. C. Johnson, A. Delgado, M. B. Raschke, F. Herrera, *J. Chem. Phys.* **2022**, *156*, 124110.
[5] A. Barulin, P. Roy, J.-B. Claude, J. Wenger, *Nat. Commun.* **2022**, *13*, 1842.
[6] A. Pályi, P. R. Struck, M. Rudner, K. Flensberg, G. Burkard, *Phys. Rev. Lett.* **2012**, *108*, 206811.
[7] V. Kravets, F. Schedin, R. Jalil, L. Britnell, R. Gorbachev, D. Ansell, B. Thackray, K. Novoselov, A. Geim, A. V. Kabashin, A. N. Grigorenko, *Nat. Mater.* **2013**, *12*, 304.
[8] R. Chikkaraddy, B. De Nijs, F. Benz, S. J. Barrow, O. A. Scherman, E. Rosta, A. Demetriadou, P. Fox, O. Hess, J. J. Baumberg, *Nature* **2016**, *535*, 127.
[9] G. M. Akselrod, C. Argyropoulos, T. B. Hoang, C. Ciracì, C. Fang, J. Huang, D. R. Smith, M. H. Mikkelsen, *Nat. Photonics* **2014**, *8*, 835.
[10] K. J. Vahala, *Nature* **2003**, *424*, 839.
[11] E. Orgiu, J. George, J. Hutchison, E. Devaux, J. Dayen, B. Doudin, F. Stellacci, C. Genet, J. Schachenmayer, C. Genes, G. Pupillo, P. Samorì, T. W. Ebbesen, *Nat. Mater.* **2015**, *14*, 1123.
[12] D. G. Baranov, M. Wersall, J. Cuadra, T. J. Antosiewicz, T. Shegai, *ACS Photonics* **2018**, *5*, 24.
[13] A. Shalabney, J. George, J. A. Hutchison, G. Pupillo, C. Genet, T. W. Ebbesen, *Nat. Commun.* **2015**, *6*, 5981.
[14] J. P. Long, B. Simpkins, *ACS Photonics* **2015**, *2*, 130.
[15] A. B. Grafton, A. D. Dunkelberger, B. S. Simpkins, J. F. Triana, F. J. Hernández, F. Herrera, J. C. Owrutsky, *Nat. Commun.* **2021**, *12*, 214.
[16] A. D. Dunkelberger, R. B. Davidson, W. Ahn, B. S. Simpkins, J. C. Owrutsky, *J. Phys. Chem. A* **2018**, *122*, 965.
[17] A. Komarov, G. Slepyan, *Appl. Sci.* **2018**, *8*, 951.
[18] A. D. Dunkelberger, C. T. Ellis, D. C. Ratchford, A. J. Giles, M. Kim, C. S. Kim, B. T. Spann, I. Vurgaftman, J. G. Tischler, J. P. Long, O. J. Glembocki, J. C. Owrutsky, J. D. Caldwell, *Nat. Photonics* **2018**, *12*, 50.
[19] J. Huang, A. J. Traverso, G. Yang, M. H. Mikkelsen, *ACS Photonics* **2019**, *6*, 838.
[20] Q.-Y. Lin, Z. Li, K. A. Brown, M. N. OBrien, M. B. Ross, Y. Zhou, S. Butun, P.-C. Chen, G. C. Schatz, V. P. Dravid, K. Aydin, C. A. Mirkin, *Nano Lett.* **2015**, *15*, 4699.

[21] R. Arul, K. Menghrajani, M. S. Rider, R. Chikkaraddy, W. L. Barnes, J. J. Baumberg, *Phys. Rev. Lett.* **2023**, *131*, 126902.
[22] A. Bylinkin, M. Schnell, M. Autore, F. Calavalle, P. Li, J. Taboada-Gutierrez, S. Liu, J. H. Edgar, F. Casanova, L. E. Hueso, P. Alonso-Gonzalez, A. Y. Nikitin, R. Hillenbrand, *Nat. Photonics* **2021**, *15*, 197.
[23] S. Campione, A. Benz, J. F. Klem, M. B. Sinclair, I. Brener, F. Capolino, *Phys. Rev. B* **2014**, *89*, 165133.
[24] G. Lerario, D. Ballarini, A. Fieramosca, A. Cannavale, A. Genco, F. Mangione, S. Gambino, L. Dominici, M. De Giorgi, G. Gigli, D. Sanvitto, *Light: Sci. Appl.* **2017**, *6*, e16212.
[25] R. Sarma, N. Nookala, K. J. Reilly, S. Liu, D. de Ceglia, L. Carletti, M. D. Goldflam, S. Campione, K. Sapkota, H. Green, G. T. Wang, J. Klem, M. B. Sinclair, M. A. Belkin, I. Brener, *Nano Lett.* **2020**, *21*, 367.
[26] J. George, A. Shalabney, J. A. Hutchison, C. Genet, T. W. Ebbesen, *J. Phys. Chem. Lett.* **2015**, *6*, 1027.
[27] K. Nagarajan, A. Thomas, T. W. Ebbesen, *J. Am. Chem. Soc.* **2021**, *143*, 16877.
[28] R. Wilcken, J. Nishida, J. F. Triana, A. John-Herpin, H. Altug, S. Sharma, F. Herrera, M. B. Raschke, *Proc. Natl. Acad. Sci.* **2023**, *120*, e2220852120.
[29] B. Metzger, E. Muller, J. Nishida, B. Pollard, M. Hentschel, M. B. Raschke, *Phys. Rev. Lett.* **2019**, *123*, 153001.
[30] C.-F. Wang, T. G. Habteyes, T. S. Luk, J. F. Klem, I. Brener, H.-T. Chen, O. Mitrofanov, *Nano Lett.* **2019**, *19*, 4620.
[31] M. Malerba, S. Sotgiu, A. Schirato, L. Baldassarre, R. Gillibert, V. Giliberti, M. Jeannin, J.-M. Manceau, L. Li, A. G. Davies, E. H. Linfield, A. Alabastri, M. Ortolani, R. Colombelli, *ACS Nano* **2022**, *16*, 20141.
[32] R. Gillibert, M. Malerba, D. Spirito, V. Giliberti, L. Li, A. G. Davies, E. H. Linfield, L. Baldassarre, R. Colombelli, M. Ortolani, *Appl. Phys. Lett.* **2020**, *117*, 10.
[33] J. Lee, M. Tymchenko, C. Argyropoulos, P.-Y. Chen, F. Lu, F. Demmerle, G. Boehm, M.-C. Amann, A. Alu, M. A. Belkin, *Nature* **2014**, *511*, 65.
[34] J. Lee, N. Nookala, J. S. Gomez-Diaz, M. Tymchenko, F. Demmerle, G. Boehm, M.-C. Amann, A. Alù, M. A. Belkin, *Adv. Opt. Mater.* **2016**, *4*, 664.
[35] S. A. Mann, N. Nookala, S. C. Johnson, M. Cotrufo, A. Mekawy, J. F. Klem, I. Brener, M. B. Raschke, A. Alù, M. A. Belkin, *Optica* **2021**, *8*, 606.
[36] S. Pirotta, N.-L. Tran, A. Jollivet, G. Biasiol, P. Crozat, J.-M. Manceau, A. Bousseksou, R. Colombelli, *Nat. Commun.* **2021**, *12*, 799.
[37] H. Chung, I. Hwang, J. Yu, G. Boehm, M. A. Belkin, J. Lee, *Adv. Sci.* **2023**, *10*, 2207520.
[38] H. Dely, T. Bonazzi, O. Spitz, E. Rodriguez, D. Gacemi, Y. Todorov, K. Pantzas, G. Beaudoin, I. Sagnes, L. Li, A. G. Davies, E. H. Linfield, F. Grillot, A. Vasanelli, C. Sirtori, *Laser Photonics Rev.* **2022**, *16*, 2100414.
[39] M. Montes Bajo, J.-M. Chauveau, A. Vasanelli, A. Delteil, Y. Todorov, C. Sirtori, A. Hierro, *J. Appl. Phys.* **2023**, *134*, 1.
[40] B. S. Simpkins, A. D. Dunkelberger, I. Vurgaftman, *Chem. Rev.* **2023**, *123*, 5020.
[41] E. A. Muller, B. Pollard, H. A. Bechtel, R. Adato, D. Etezadi, H. Altug, M. B. Raschke, *ACS Photonics* **2018**, *5*, 3594.
[42] K. Wang, M. Seidel, K. Nagarajan, T. Chervy, C. Genet, T. Ebbesen, *Nat. Commun.* **2021**, *12*, 1486.
[43] C. Garrido Alzar, M. Martinez, P. Nussenzveig, *Am. J. Phys.* **2002**, *70*, 37.
[44] M. Fleischhauer, A. Imamoglu, J. P. Marangos, *Rev. Mod. Phys.* **2005**, *77*, 633.
[45] H. A. Bechtel, E. A. Muller, R. L. Olmon, M. C. Martin, M. B. Raschke, *Proc. Natl. Acad. Sci.* **2014**, *111*, 7191.
[46] R. Hillenbrand, T. Taubner, F. Keilmann, *Nature* **2002**, *418*, 159.
[47] N. Ocelic, A. Huber, R. Hillenbrand, *Appl. Phys. Lett.* **2006**, *89*, 101124.
[48] L. Mester, A. A. Govyadinov, R. Hillenbrand, *Nanophotonics* **2022**, *11*, 377.
[49] P. Törmä, W. L. Barnes, *Rep. Prog. Phys.* **2014**, *78*, 013901.
[50] P. A. Thomas, W. J. Tan, H. A. Fernandez, W. L. Barnes, *Nano Lett.* **2020**, *20*, 6412.
[51] R. H. Pantell, H. E. Puthoff, *Fundamentals of quantum electronics*, John Wiley & Sons, Hoboken, New Jersey **1969**.
[52] M. Mondal, A. Semenov, M. A. Ochoa, A. Nitzan, *J. Phys. Chem. Lett.* **2022**, *13*, 9673.
[53] M. Autore, P. Li, I. Dolado, F. J. Alfaro-Mozaz, R. Esteban, A. Atxabal, F. Casanova, L. E. Hueso, P. Alonso-González, J. Aizpurua, A. Y. Nikitin, S. Vélez, R. Hillenbrand, *Light: Sci. Appl.* **2018**, *7*, 17172.
[54] I. Dolado, C. Maciel-Escudero, E. Nikulina, E. Modin, F. Calavalle, S. Chen, A. Bylinkin, F. J. Alfaro-Mozaz, J. Li, J. H. Edgar, F. Casanova, S. Vélez, L. E. Hueso, R. Esteban, J. Aizpurua, R. Hillenbrand, *Nat. Commun.* **2022**, *13*, 6850.
[55] G. Günter, A. A. Anappara, J. Hees, A. Sell, G. Biasiol, L. Sorba, S. De Liberato, C. Ciuti, A. Tredicucci, A. Leitenstorfer, R. Huber, *Nature* **2009**, *458*, 178.
[56] E. B. Dunkelberger, M. Grechko, M. T. Zanni, *J. Phys. Chem. B* **2015**, *119*, 14065.
[57] P. Lazzeretti, R. Zanasi, W. T. Raynes, *J. Chem. Phys.* **1987**, *87*, 1681.
[58] P. Pons-Valencia, F. J. Alfaro-Mozaz, M. M. Wiecha, V. Biolek, I. Dolado, S. Vélez, P. Li, P. Alonso-González, F. Casanova, L. E. Hueso, L. Martín-Moreno, R. Hillenbrand, A. Y. Nikitin, *Nat. Commun.* **2019**, *10*, 3242.
[59] R. Houdré, J. Gibernon, P. Pellandini, R. Stanley, U. Oesterle, C. Weisbuch, J. O'Gorman, B. Roycroft, M. Ilegems, *Phys. Rev. B* **1995**, *52*, 7810.
[60] J. George, T. Chervy, A. Shalabney, E. Devaux, H. Hiura, C. Genet, T. W. Ebbesen, *Phys. Rev. Lett.* **2016**, *117*, 153601.
[61] A. Dunkelberger, B. Spann, K. Fears, B. Simpkins, J. Owrutsky, *Nat. Commun.* **2016**, *7*, 13504.